A Rh_xS_y/C Catalyst for the Hydrogen Oxidation and Hydrogen Evolution Reactions in HBr

Jahangir Masud,[a,*] Trung Van Nguyen,[a,,z] Nirala Singh,[b] Eric McFarland,[b,*] Myles Ikenberry,[c] Keith Hohn,[c] Chun-Jern Pan,[d] and Bing-Joe Hwang[d,*]**

[a]*Department of Chemical & Petroleum Engineering, The University of Kansas, Lawrence, Kansas 660445, USA*
[b]*Department of Chemical Engineering, University of California, Santa Barbara, California 93106, USA*
[c]*Department of Chemical Engineering, Kansas State University, Manhattan, Kansas 93106, USA*
[d]*Department of Chemical Engineering, National Taiwan University of Science & Technology, Taipei, Taiwan*

Rhodium sulfide (Rh_2S_3) on carbon support was synthesized by refluxing rhodium chloride with ammonium thiosulfate. Thermal treatment of Rh_2S_3 at high temperatures (600°C to 850°C) in presence of argon resulted in the transformation of Rh_2S_3 into Rh_3S_4, $Rh_{17}S_{15}$ and Rh which were characterized by TGA/DTA, XRD, EDX, and deconvolved XPS analyses. The catalyst particle size distribution ranged from 3 to 12 nm. Cyclic voltammetry and rotating disk electrode measurements were used to evaluate the catalytic activity for hydrogen oxidation and evolution reactions in H_2SO_4 and HBr solutions. The thermally treated catalysts show high activity for the hydrogen reactions. The exchange current densities *(i_o)* of the synthesized Rh_xS_y catalysts in H_2-saturated 1M H_2SO_4 and 1M HBr for HER and HOR were 0.9 mA/cm^2 to 1.0 mA/cm^2 and 0.8 to 0.9 mA/cm^2, respectively. The lower i_o values obtained in 1M HBr solution compared to in H_2SO_4 might be due to the adsorption of Br^- on the active surface. Stable electrochemical active surface area (ECSA) of RhxSy catalyst was obtained for CV scan limits between 0 V and 0.65 V vs. RHE. Scans with upper voltage limit beyond 0.65 V led to decreased and unreproducible ECSA measurements.
 [DOI: 10.1149/2.0901504jes]

Manuscript submitted December 22, 2014; revised manuscript received January 30, 2015. Published February 10, 2015.

The intermittent availability of renewable electricity from solar and wind sources has increased significantly.[1] To match their often unpredictable power generation cycles with demand, low cost electrical energy storage systems are required.

A flow battery/regenerative fuel cell is an electrochemical storage device that stores the electrical energy as chemical energy in a fuel and converts the chemical energy of the fuel directly back to electrical energy. The potentially low cost and relatively rapid process of electrical-to-chemical or chemical-to-electrical energy, in comparison to the slower mechanical-to-electrical energy processes used with flywheel and compressed air storage, offers unique advantages. The discharge cycle of the flow battery utilizes a fuel cell which has proven to be efficient and clean devices for energy conversion. Fuel cells are regarded by some as the energy conversion devices of the future and provide a faster, cleaner, more efficient, and possibly more flexible chemical-to-electrical energy conversion platform than present combustion based systems.[2–4]

In comparison to other flow battery systems, the regenerative hydrogen-bromine fuel cell has advantages including high round-trip energy conversion efficiency, high power density and storage capacity, fast kinetics of both hydrogen and bromine electrode reactions, low cost active materials, simplicity and reliability.[5–6] The core component of a H_2/Br_2 regenerative fuel cell system is an acid-based H_2/Br_2 fuel cell. The charge and discharge reactions occurring in the fuel cell are as follows. At the bromine electrode, during the charge cycle, bromide ions in an HBr solution are oxidized to form bromine and two electrons;

$$2HBr \underset{\text{charge}}{\overset{\text{discharge}}{\rightleftharpoons}} 2H^+ + Br_2 + 2e^-, \quad E^0 = 1.09\,V$$

The standard reduction potential for this reaction is 1.09 V. The hydronium ions migrate across proton conducting membrane to the hydrogen side of the fuel cell and are reduced to H_2,

$$2H^+ + 2e^- \underset{\text{charge}}{\overset{\text{discharge}}{\rightleftharpoons}} H_2, \quad E^0 = 0.00\,V$$

While no precious metals are needed to catalyze the bromine reactions, the hydrogen oxidation and evolution (HOR/HER) reactions require a catalyst that is highly active, to keep the performance high and the cost low, stable and durable in the highly corrosive HBr/Br_2 environment of the cell as required by the extended life of this application. During the operation of a H_2-Br_2 fuel cell, HBr and Br_2 could cross from the bromine side through the proton conducting membrane to the hydrogen side potentially leading to the corrosion and poisoning of the catalyst used at the hydrogen electrode. The highly active HER/HOR platinum catalyst that is currently used in the acid-based hydrogen-oxygen fuel cells is not stable in the HBr/Br_2 environment.[6–7] Consequently, alternative HER/HOR catalyst materials are needed for this system. Rhodium sulfide catalysts have shown promise in applications for hydro-desulfurization,[8–9] photochemical decomposition of aqueous sulfide[10] and the oxygen reduction reaction (ORR) for fuel cells and electrolysis.[11–18] In the particular case of hydrochloric acid electrolysis, Pt, known as the most effective catalyst for non-chloride systems, has been shown to have poor stability in the highly corrosive conditions of hydrochloric acid and be constantly poisoned by chloride ions. In contrast, rhodium sulfides are relatively unaffected by chloride ions. More recently, our group has found[6] that rhodium sulfides could be a promising candidate for hydrogen catalysis due to its high stability in HBr / Br_2 environment. The active phases are believed to be Rh_3S_4, $Rh_{17}S_{15}$, and Rh.[19–20]

In this work, rhodium sulfide catalysts were synthesized on carbon supports and characterized by transmission electron microscopy (TEM) and X-ray diffraction (XRD), X-ray Photoelectron spectroscopy (XPS) and Energy-dispersive X-ray spectroscopy (EDX) techniques. Cyclic voltammetry (CV) was used for electrochemical characterization and electrochemically active surface area (ECSA) measurement. The HER/HOR activities were investigated in H_2SO_4 and HBr solutions by multi-potential step method.

Experimental

Catalyst synthesis.— The synthesis procedure for rhodium sulfide precursor on carbon support (Rh_2S_3/C, Rh:C weight ratio 1:3) catalyst can be found in the patent literature.[21] The carbon support used in this study was Vulcan XC-72. This electrochemically inactive precursor was thermally treated in a quartz oven at different definite temperatures in the presence of argon to make active phases (Rh_3S_4, $Rh_{17}S_{15}$ and Rh) containing catalysts. Thermal reduction was carried out from room temperature (RT) to 600°C, 700°C, 800°C and 850°C and all

*Electrochemical Society Active Member.
**Electrochemical Society Fellow.
zE-mail: cptvn@ku.edu

catalysts were heated at final temperature for 30 minutes. The ramp rates were as follows:

For 600°C: RT to 550°C at 10°C/min; 550 to 575°C at 2°C/min and 575 to 600°C at 1°C/min.

For 700°C: RT to 650°C at 10°C/min; 650 to 675°C at 2°C/min and 675 to 700°C at 1°C/min.

For 800°C: RT to 750°C at 10°C/min; 750 to 775°C at 2°C/min and 775 to 800°C at 1°C/min.

For 850°C: RT to 800°C at 10°C/min; 800 to 825°C at 2°C/min and 825 to 850°C at 1°C/min.

Physical characterizations.— The thermogravimetric analysis (TGA) and differential thermal analysis (DTA) were performed by Perkin Elmer Diamond TG/DTA. The morphology and chemical compositions of the samples were determined by FEI Tecnai F20 XT Field Emission Transmission Electron Microscope (TEM) coupled with an energy-dispersive X-ray spectrometer (EDX) at an acceleration voltage of 200 kV. XRD data were collected on an X'Pert powder diffractometer (PANalytical, Inc.) with a Cu Kα source (corresponding to a photon wavelength of 1.54 Å). In XPS measurements, the prepared catalysts were analyzed by a Perkin−Elmer PHI 5400 electron spectrometer with an achromatic X-ray source (Al Kα (hυ = 1486.6 eV)) anode. The XPS binding energies were measured with a precision of 0.1 eV. The analyzer pass energy was set to 17.9 eV, and the contact time was 50 ms. The spectrometer was calibrated by setting the binding energies of Au $4f_{7/2}$ and Cu $2p_{3/2}$ to 84.0 and 932.7 eV, respectively. For each measurement, all XPS spectra were corrected to the internal reference spectra of C 1s at 284.5 eV to compensate for electrostatic charging. Then, the core-level spectra were carefully deconvolved using the CasaXPS software to investigate the chemical states of elements on the electrocatalyst surface.

Electrode preparation.— The catalyst ink was prepared by ultrasonically dispersing 1.6 mg catalysts in 2.0 mL isopropyl alcohol (IPA) and the dispersion was then ultrasonicated for 30 min. Glassy carbon (GC) rotating disk electrodes, RDEs, with 5 mm diameter were polished with 0.05 μm alumina suspensions to a mirror finish before each experiment and served as an underlying conductive substrate of the working electrode. A quantity of 20 μL of the dispersion was pipetted out on the top of the GC. The catalyst layer was dried at room temperature. Then, an aliquot of Nafion solution (10 μl of 1 mg/mL solution in 50% IPA in water) was applied onto catalyst layer to yield an average film thickness of 0.25μm. The Nafion-coated working electrode was dried at room temperature and finally heated at 130°C for 30 min. in air in an oven.

Electrochemical measurements.— All electrochemical measurements were made with a Gamry Instrument (G300 Potentiostat/Galvanostat/ZRA). Electrochemical measurements were carried out in a conventional three-electrode electrochemical cell at 25°C, with the glassy carbon disk electrode made in the above mentioned procedure as the working electrode and a saturated calomel electrode (SCE) as the reference electrode. A piece of Pt foil (1 cm^2) was placed in a separate chamber to serve as the counter electrode, which was connected to the working electrode chamber through a KCl salt bridge. All solutions were prepared with ultrapure water (Millipore, 18.25 MΩ · cm). The solution of 1M H_2SO_4 was purged with N_2 gas for nearly 30 min. before starting the cyclic voltammograms. Before the electrochemical measurements, the working electrode was soaked in de-ionized (DI) water for 2 hrs to ensure that the Nafion binder is well hydrated. Fresh electrolyte solution was used for each electrochemical measurement to ensure reproducible results. All the potentials reported herein were with respect to the reversible hydrogen electrode (RHE) potential. Cyclic voltammograms were measured in N_2-saturated 1 M H_2SO_4 solution from 0 to 0.65 V vs. RHE at 20 mV s^{-1} to avoid oxidizing the materials at high potentials, which has been found to lead to inconsistent ECSA measurements. In order to prevent H_2 bubble accumulation at electrode surface, the RDE was tilted about 5 to 10 degrees and the electrode was rotated at 10 rpm. Since ECSA measured during the anodic scan is related to the charge associated with the oxidation of adsorbed hydrogen atoms on the catalyst surface only, any small variation in the dynamics of the electrolyte from a slightly tilted electrode rotating at 10 rpm is not expected to affect this measurement.

N_2-gas was passed through the electrolyte solution continuously during the CV scan. The "relative" electrochemical active specific surface area (ECSA) of catalyst "with respect to platinum" was calculated from the coulombic charges measured during the hydrogen oxidation step after correcting for double-layer charging current using the following equation:

$$\text{ECSA} = \frac{Q_H}{0.21} \quad [1]$$

where ECSA is the electrochemical active surface area in cm^2, Q_H (mC) is the charge from the oxidation of adsorbed hydrogen in the hydrogen region of the CVs, 0.21 mC/cm^2 (which is also reported for other non-Pt catalysts[22–23]) is the electrical charge associated with monolayer adsorption of hydrogen on Pt. Finally, hydrogen oxidation and hydrogen evolution (HOR/HER) was carried out at 2500 rpm in H_2-saturated 1M H_2SO_4 and 1M HBr solution by using multiple-step chronoamperometry method. The electrode was also tilted about 5–10 degrees in these measurements to prevent H_2 bubble accumulation at electrode surface. At these rotation speeds, the effect of the gravitational force, especially with the slight change in this force by tilting and for this small angle and electrode radius, on the fluid dynamics is minimal. Furthermore, only the data in the kinetically controlled region were used to determine the catalyst activity. IR compensation was done by measuring the resistance between the working electrode and reference electrode by electrochemical impedance spectroscopy.

Results and Discussion

Physical characterizations.— Thermal analysis measurement of the synthesized precursor (Rh_2S_3/C) was carried out using thermogravimetric analysis (TGA) and differential thermal analysis (DTA). The catalyst was heated from room temperature to 850°C with an increment of 5°C/min in Ar. Fig. 1 shows a plot of TGA/DTA. Notably, the TGA curve can be divided into three weight-loss steps. The first step (about 5% weight loss) from room temperature to about 400°C was due to the desorption of absorbed water molecules on the sample. The second step between 400 and 570°C shows a ∼20% weight loss, which might be due to the release of excess sulfur because of its high volatility (boiling point at 444.6°C), as 20% excess sulfur was used during the synthesis of the precursor. Finally, weight loss from 570°C to 850°C was due to the phase transformation of the Rh_2S_3 precursor. This phase transformation is supported by XRD results

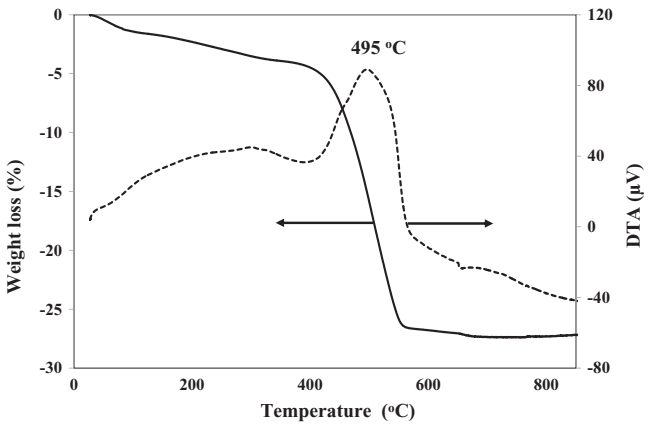

Figure 1. TGA-DTA curves of precursor (Rh_2S_3/C). Scan rate of 5°/min.

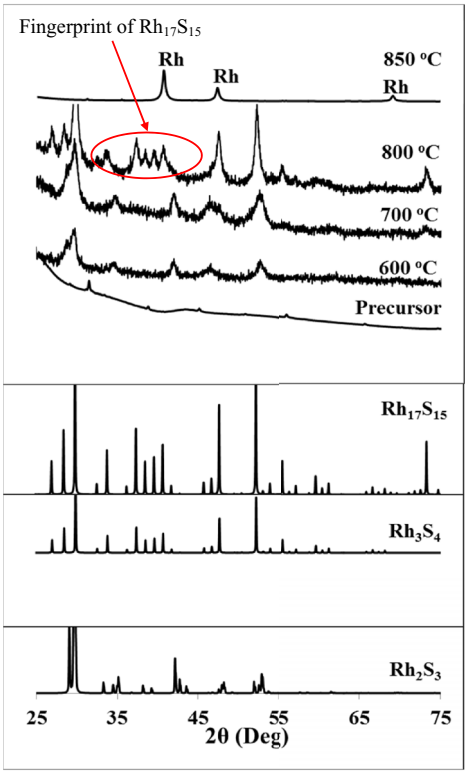

Figure 2. XRD patterns of the precursor and catalysts synthesized at 600°C, 700°C, 800°C and 850°C. The index of the phases is also shown.

which are discussed later. Within the DTA data one exothermic peak is identified at 495°C which might be assigned to the crystallization of Rh_2S_3. Similar TGA/DTA results were observed by Zhang et al.[24] during the hydrothermal synthesis of rhodium sulfides. It is clear that temperature is a key factor in controlling the phase composition of rhodium sulfide in the catalyst. To obtain the active phase composition of rhodium sulfides (Rh_3S_4, $Rh_{17}S_{15}$ and Rh), the precursor was treated from 600°C to 850°C.

The XRD of the synthesized catalysts at different temperatures shown in Fig. 2 confirmed the presence of different phases of rhodium sulfides, such as Rh_2S_3 (ICSD No.15344), Rh_3S_4 (ICSD No. 410813), $Rh_{17}S_{15}$ (ICSD No. 410838) and Rh (ICSD No.426969). The result shows that the precursor was poorly crystallized and potentially composed of Rh_2S_3 phase. However, the catalysts were crystallized after thermal treatment, and the crystallized phases of the products varied with the heat-treatment temperature. For the catalysts synthesized at 600°C and 700°C, mixtures of Rh_2S_3 and $Rh_{17}S_{15}$ phases were obtained. The catalyst synthesized at 700°C contained more of the $Rh_{17}S_{15}$ phase than was observed in the 600°C synthesized catalyst. Synthesis at 800°C resulted in samples composed of mostly the $Rh_{17}S_{15}$ phase with a small amount of Rh_2S_3 and Rh phases. It is noted that the diffraction spectra between 31° to 42° clearly mark the fingerprint of $Rh_{17}S_{15}$ phase. The XRD pattern of the sample at 850°C was dominated by elemental Rh phase. As the XRD spectrum of Rh_3S_4 is almost superimposed with the spectrum of $Rh_{17}S_{15}$ (see the reference spectrum in Fig. 2), it is difficult to index them. These results indicate that the Rh_2S_3 material was transformed to other phases by loss of sulfur during thermal reduction. Similar thermal treatment phenomenon for rhodium sulfide catalyst was also reported.[16,24]

The average catalyst particle size was calculated from the XRD diffraction peak width using the Scherer equation:[25]

$$L = \frac{K\lambda}{\beta Cos\theta} \quad [2]$$

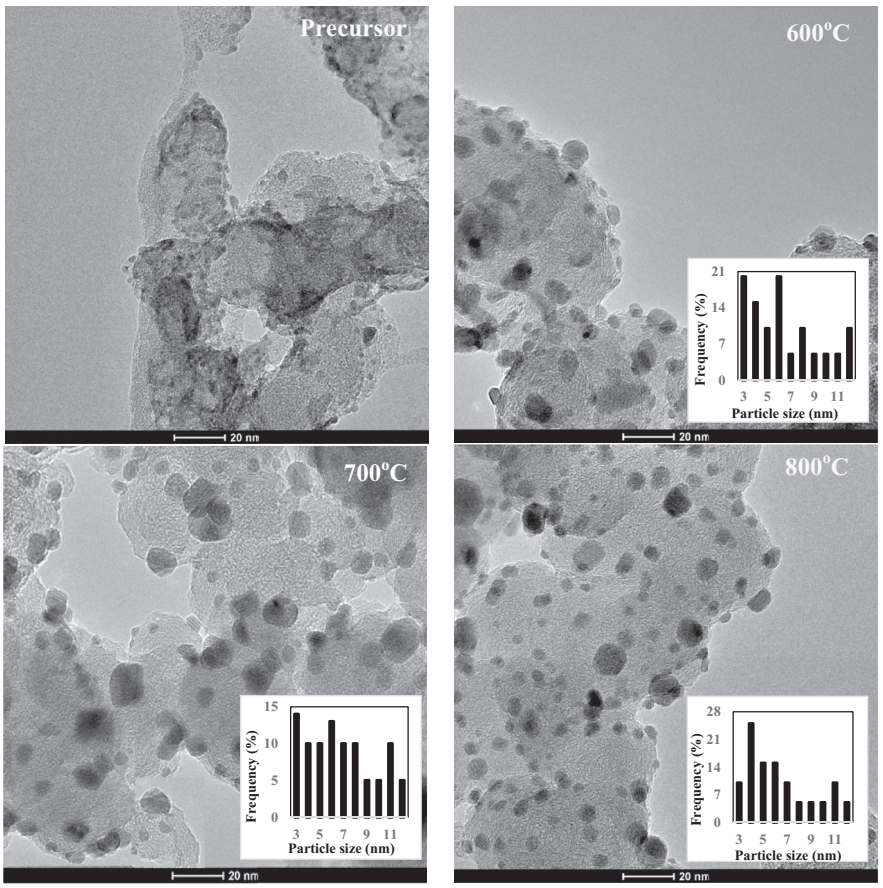

Figure 3. TEM images of catalyst precursor, Rh_2S_3/C and after thermal treatment at 600°C, 700°C, and 800°C. The corresponding histograms of particle size distributions were plotted in the insets.

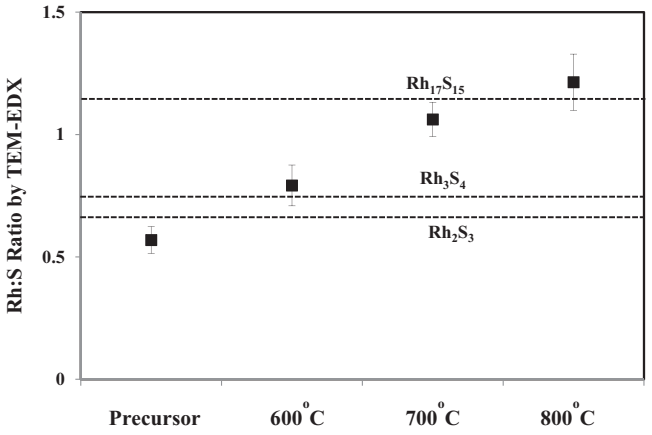

Figure 4. Rh to S ratio of catalysts obtained by TEM-EDX.

where L is the particle size, λ is the X-ray wavelength in nanometer (0.15418 nm), β is the peak width of the diffraction peak profile at half maximum height in radians and *K* is a constant, normally taken as 0.9. The value of β in 2θ axis of diffraction profile must be in radians. We were unable to calculate the average particle size for the poorly crystallized Rh_2S_3 precursor phase. The particle sizes for both the 600°C and 700°C catalysts are 8.7 nm, 9.9 nm for the 800°C catalyst and 19.9 nm for the 850°C catalyst, respectively. The increase in particle size with temperature might be attributed to the migration and agglomeration of catalyst at higher temperature. To avoid the formation of elemental Rh, we limited the catalyst synthesis temperature to 800°C for the thermal reduction in the rest of study.

The morphology and distribution of the catalysts were evaluated by TEM. Fig. 3 shows TEM images of the precursor (Rh_2S_3/C) and thermally reduced catalysts. The carbon particles are the 40 nm objects, with the Rh_xS_y as the darker particles. Well-defined crystallites and particle size distribution were not observed for untreated Rh_2S_3/C precursor. After thermal treatment of the precursor, consistent particle size distribution was observed (at 600°C, 700°C and 800°C). The particle size was measured directly from the TEM images at different randomly selected regions of each sample. Histograms of the particle size distributions of Rh_xS_y catalysts are included as insets in Fig 3. Similar particle size distribution on the order of 3–12 nm (mean of 6 nm) of all catalysts was found on carbon support, some agglomeration of individual crystals was noted. These catalyst particle sizes are in good agreement with the XRD results.

EDX was used to measure the elemental compositions and the rhodium to sulfur atomic ratios of these catalysts, and the results are shown in Figure 4. The Rh:S atomic ratio for the precursor was about 0.57 which is slightly lower than the theoretical atomic ratio of Rh_2S_3 (0.67) indicating the presence of some elemental sulfur in the catalyst. The Rh:S ratio was found to increase upon thermal treatment. It is noteworthy to point out that Rh:S ratios greater than 1.13, such as that synthesized at 800°C (1.21), are due to the formation of elemental Rh. The electronic states of Rh in Rh_xS_y/C catalysts were studied by XPS, and the results are shown in Fig. 5. Figure 5a shows that the binding energies of 3d levels of Rh in different catalysts were shifted to higher values (i.e., 309.2 [$3d_{5/2}$] and 314.2 [$3d_{3/2}$] eV for the precursor; 308.9 [$3d_{5/2}$] and 313.9 [$3d_{3/2}$] eV for 600°C; 308.5 [$3d_{5/2}$] and 313.0 [$3d_{3/2}$] eV for 700°C and 307.8 [$3d_{5/2}$] and 312.9 [$3d_{3/2}$] eV for catalyst 800°C) in comparison with those (307 [$3d_{5/2}$] and 312 [$3d_{3/2}$] eV) of elemental Rh. This indicates that Rh existed in a cationic state rather than in an elemental state in these catalysts. Figure 5b shows the XPS spectra of O1s. The peak at 532 eV is due to the presence of oxygen-containing groups on the carbon surface.[26] Oxidic rhodium (at ca. 530 eV[27]) is not detected in any of these catalysts, thus ruling out the formation of rhodium oxide. As shown in Fig. 5c, the contributions at ca. 162.1 eV at the lower binding energy portion of the S 2p peak originate from $S^{\delta-}$ present in sulfide[28–29] and are clearly visible in all

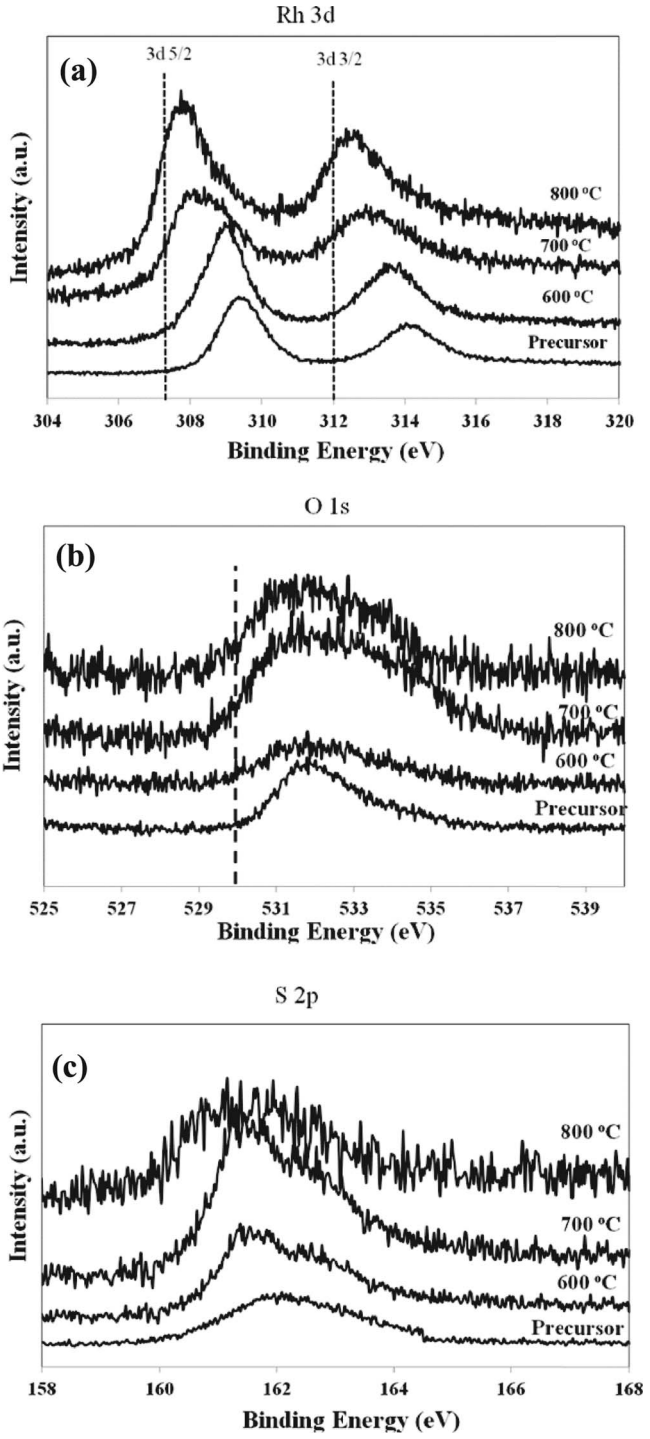

Figure 5. XPS spectra of catalysts precursor, and after thermal treatment at 600°C, 700°C, 800°C: (a) Rh 3d, (b) O1s and (c) S2p.

samples. In the precursor, the shoulder at higher binding energy at around 164 eV implies the existence of elemental sulfur, in accord with the EDX results. This is an indication that excess S higher than the stoichiometric ratio of 1.50 in the composite exists as elemental sulfur.

In order to investigate the different phases within the samples, Rh3d spectra are carefully deconvolved and presented in Fig. 6. The binding energy observed for Rh3d in the precursor (Fig. 6a) shows a doublet at 309.2 eV and 314.2 eV, corresponding to $3d_{5/2}$ and $3d_{3/2}$ states, respectively. Normally, the peak at 309.2 eV arises from covalently bound oxidized Rh (sulfide and/or oxide, but we can exclude

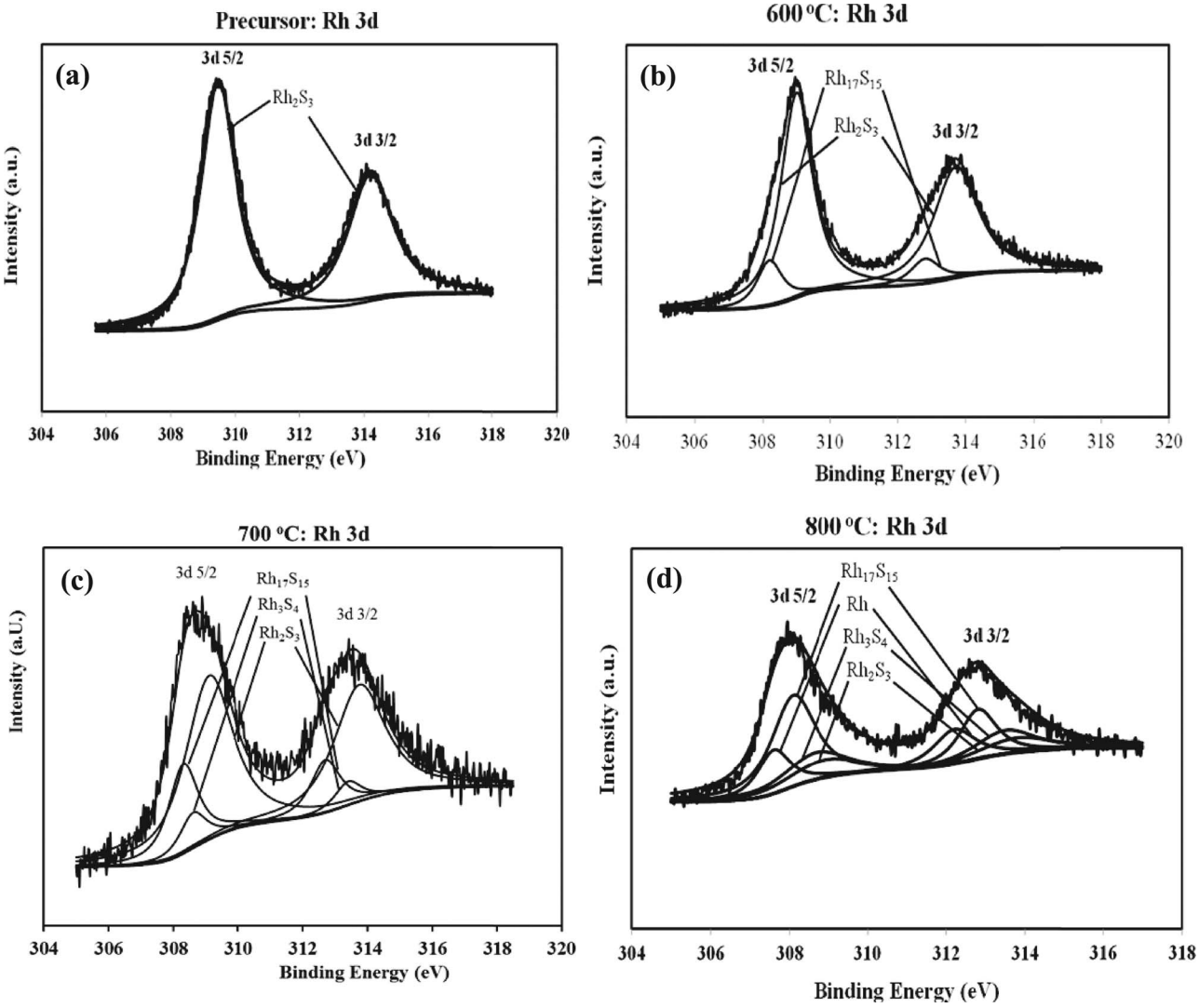

Figure 6. Deconvolved XPS Rh3d spectra of (a) precursor (b) 600°C (c) 700°C and (c) 800°C.

the possibility of rhodium oxide as no O 1s peak is found at 530 eV). Combined with S 2P analysis, these peaks are attributed to covalently bonded, sulfurized Rh (Rh_2S_3) which is also evident from XRD result. However, it is noted the Rh_2S_3 can be transformed to Rh_3S_4, $Rh_{17}S_{15}$ and Rh by loss of sulfur during thermal reduction in presence of Ar (from XRD results). Deconvolution spectrum of $Rh3d_{5/2}$ in Fig. 6b for 600°C shows the presence of a small amount of $Rh_{17}S_{15}$ phase (ca. 308.2 eV) whereas the main contributor of the spectrum is Rh_2S_3 (ca. 309.2 eV). Similar deconvolved spectra is observed for the catalyst at 700°C (Fig. 6c) where the main peaks are due to Rh_2S_3 (ca. 309.2 eV) with $Rh_{17}S_{15}$ (ca. 308.2 eV) and Rh_3S_4 (ca. 308.7 eV). As demonstrated in Fig. 6d for the 800°C sample, the spectrum of the lowest binding energy of Rh $3d_{5/2}$ is 1.2 eV lower than that of Rh_2S_3. This shift confirms that at relatively high temperature, Rh_2S_3 is transformed to other phases, mainly $Rh_{17}S_{15}$ (ca. 308.2 eV) with a small amount of Rh_3S_4 (ca. 308.7 eV) and Rh (ca. 307.3 eV). However, a small peak at ca. 309.2 eV, which corresponds to Rh_2S_3, is also observed indicating that some Rh_2S_3 remained. The different phase compositions of the catalysts are calculated from the area of deconvolved peaks and summarized in Table I.

Cyclic voltammograms.— Previous studies[16,30–31] had reported cyclic voltammograms (CV) in N_2-saturated H_2SO_4 solution of Rh_xS_y/C from 0 to 1.2 V (vs. RHE) and that electrochemical active surface area (ECSA) measurements by CV had been problematic. Similarly, we have found inconsistent relative ECSA, with respect to polycrystalline Pt surface, when CV was scanned at this potential range. To resolve this issue, we have measured the CVs in N_2-saturated 1M H_2SO_4 solution of Rh_xS_y/C at different anodic potential limit to get consistent and reproducible ECSA. A family of cyclic voltammograms of Rh_xS_y/C in 1M H_2SO_4 is shown in Fig. 7a. The anodic limit was increased progressively on each sweep after the electrode was cleaned from 0 to 1.0 V (vs. RHE) for 2 cycles at a scan rate of 100 mV s^{-1} at the beginning of each sweep. After the final anodic limit, an additional CV scan was conducted from 0 to 0.6 V (dotted line) to check the reproducibility of results. Electrochemical active surface area (relative to Pt) of each sweep was calculated and summarized in the inset of Fig. 7b. Interestingly, the ECSA was found to decrease as the potential window was extended in the positive direction. This phenomenon might be due to the formation

Table I. Phase composition of synthesized catalysts.

Phases	Precursor (%)	600°C (%)	700°C (%)	800°C (%)
Rh	-	-	-	16
$Rh_{17}S_{15}$	-	15	35	52
Rh_3S_4	-	-	12	15
Rh_2S_3	100	85	53	17

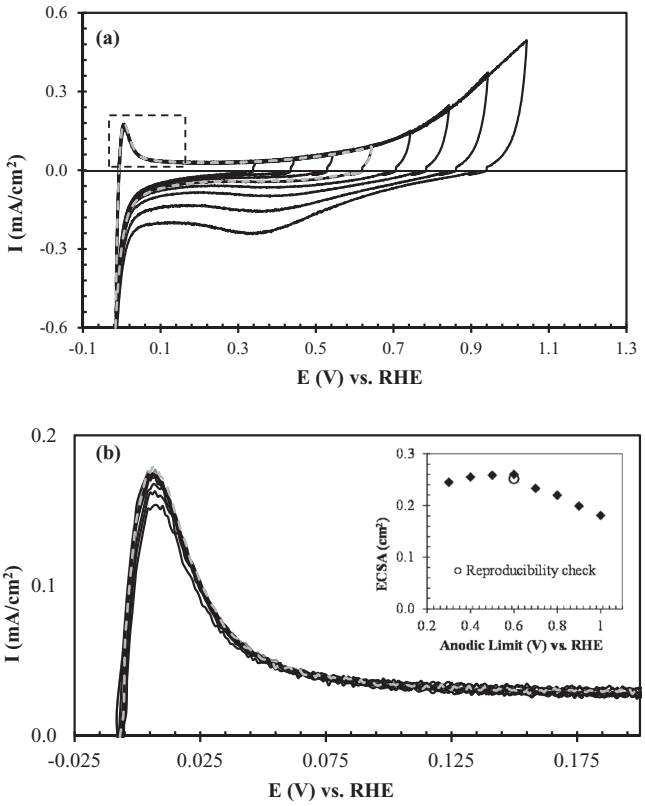

Figure 7. (a) CVs of Rh_xS_y/C (800°C) electrode in N_2-saturated 1M H_2SO_4 solution with different anodic potential limits. Potential scan rate: 0.02 V s^{-1}. (b) Enlarged CVs of Fig. 7a (dotted rectangular) and inset is the plot of ECSAs calculated at different anodic limits.

and adsorption of OH ions on Rh sites of the catalyst and formation of rhodium hydrous oxide species which could not be reduced during the cathodic scan. The formation of these species can suppress the hydrogen adsorption/desorption on the electrode surface. Furthermore, the double-layer charging current was found to increase with increasing anodic potential limit which could indicate the incomplete reduction of adsorbed oxides species at the Rh_xS_y surface. Thus, in this study, we have performed the CV scan from 0 to 0.65 V (vs. RHE) to avoid the interference of oxide/hydroxide formation and reduction that lead to inconsistent ECSA.

Figure 8 shows CVs of the precursor, 600°C, 700°C and 800°C catalysts in N_2-saturated 1M H_2SO_4 solution at 25°C. With the exception of the precursor, the catalysts showed a similar behavior with well-defined hydrogen adsorption/desorption peaks. No peak corresponding to hydrogen adsorption/desorption was observed for the precursor. Relative ECSA with respect to Pt surface was calculated and the highest ECSA was obtained for 800°C, in agreement with the XRD/XPS results which showed that the 800°C contained the highest composition of active phases (Rh_3S_4, $Rh_{17}S_{15}$, Rh) active phase composition. ECSAs of these catalysts are presented in Table II.

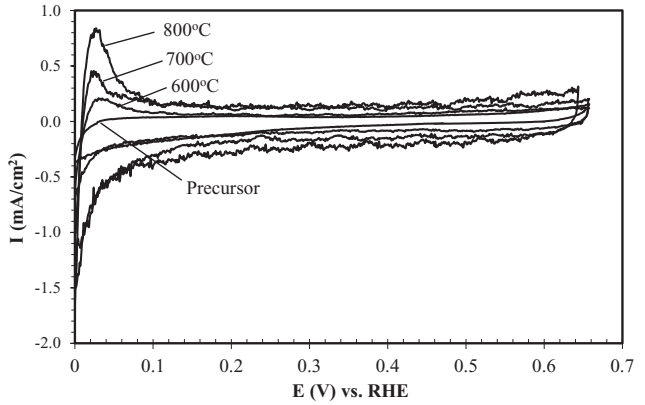

Figure 8. CVs measured at different catalysts in N_2-saturated 1M H_2SO_4 solution at a scan rate of 20 mV s^{-1}.

Table II. ECSA of different catalysts.

Catalysts	ECSA (cm^2/mg-Rh)
Precursor	-
600°C	26.27 ± 0.23
700°C	58.05 ± 0.26
800°C	186.32 ± 0.41

HOR/HER activity.— The electrode current for the HOR and HER reactions can approximately be represented by a Butler-Volmer relation with no mass transport resistance as follows:

$$i = ai_o \left\{ \left[exp \frac{a_a F}{RT} (\eta) \right] - \left[exp \frac{-a_c F}{RT} (\eta) \right] \right\} \quad [3]$$

where i represents the measured current density in A per cm^2 of geometric area, a is the catalyst area per geometric area, i_o is the exchange current density in A per cm^2 of catalyst area, α_a and α_c are the anodic and cathodic transfer coefficients, F is Faraday's constant, R is the universal gas constant, T is temperature, and $\eta = E\text{-}E_{eq}$ is the overpotential. The exchange current density (i_o) is an important kinetic parameter representing the catalytic activity of a catalyst. The Butler-Volmer equation above can be simplified when the value of η is sufficiently small, ($|\eta| < 25$ mV):

$$i \cong ai_o \left\{ (a_a + a_c) \left(\frac{F}{RT} \eta \right) \right\} \cong ai_o \frac{nF}{RT} \eta \quad [4]$$

From the slope of I versus η curve, i_o can be calculated as shown in equation 4.

The evaluation of the experimental current I vs. η for the hydrogen oxidation and hydrogen evolution reaction on Rh_xS_y/C electrode was carried out in 1M H_2SO_4 as well as 1M HBr solution under hydrogen atmosphere at rotation rate of 2500 rpm. After the open circuit voltage (OCV) reached the equilibrium value (0.0 ± 0.0002 V vs. RHE), multi potential steps (each step was for 10 s) were applied in increments of 0.002 V from OCV to ±0.016 V. Chronoamperometric response of the electrode in 1M H_2SO_4 is shown in Fig. 9. It can be observed that the current quickly reached steady state, as expected at these low current densities. Readings of the current value were made every 1 s and the mean value of the current data measured in the last 5 s

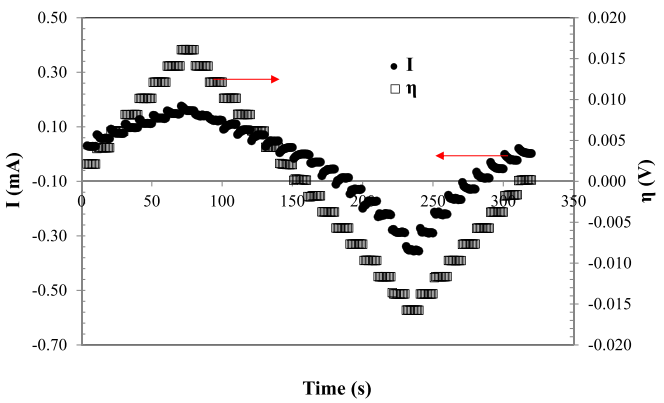

Figure 9. Chronoamperometric results of catalyst 800°C at various applied potentials.

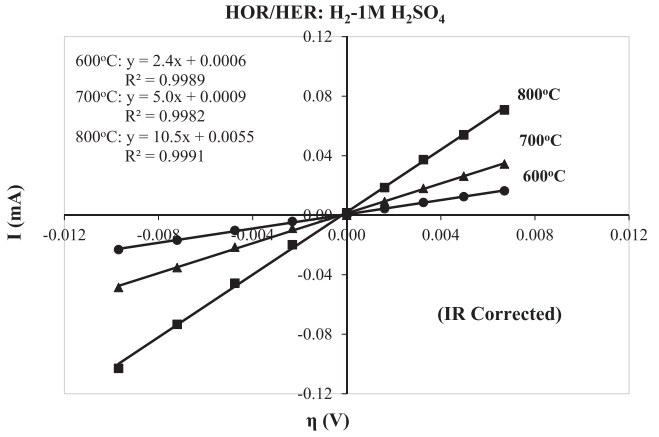

Figure 10. Linear plots of current density versus applied potentials of synthesized catalysts in H_2-saturated 1M H_2SO_4 solution.

of each potential step was used to create the current density versus overpotential plots shown in Figures 10 and 11 for 1M H_2SO_4 and 1M HBr, respectively. The exchange current densities of the catalysts were obtained from the slopes of the *I* vs. η lines and summarized in Table III. Note that conversion of the current to the current density is not necessary because *i* and *a* in Equations 3 and 4 are both referenced to the same geometric area.

Exchange current density (i_o) per active area is an intrinsic property of the catalyst. In this case where multiple active phases are present, the measured exchange current densities represent the average values of all the active phases. The fact that the exchange current densities are almost the same says that the active phase is probably the same for all three samples. It might not be certain that it is $Rh_{17}S_{15}$, but the fact that the ECSA is increasing with $Rh_{17}S_{15}$ indicates that $Rh_{17}S_{15}$ is likely to be contributing to activity. Catalyst synthesized at 800°C gave the highest mass specific exchange current density as it was composed of the maximum fraction of active phases. The i_o in 1M HBr for all catalysts were found to be lower those obtained in 1M H_2SO_4 solution. For Pt,[7,32] this is known to be due to the adsorption of Br^- on the active surface, so it is possible a similar effect is seen here. The slightly higher exchange current density for the 800°C catalyst could be attributed to the formation of the higher activity Rh phase, which exists at 15% in this sample.

It has been reported[19] that the bifunctional HOR/HER activities of supported Rh_xS_y were due to undefined synergistic effect of the conductive Rh_3S_4 and $Rh_{17}S_{15}$ phases in the catalyst (Rh_2S_3 is a semiconductor). Similarly, it is evident from XPS results of the catalyst that as the active phase composition (mixture of Rh_3S_4, $Rh_{17}S_{15}$ and Rh) increases with increasing pretreatment temperature, from 600°C to 800°C, the bifunctional HOR/HER activity was also found to increase accordingly.

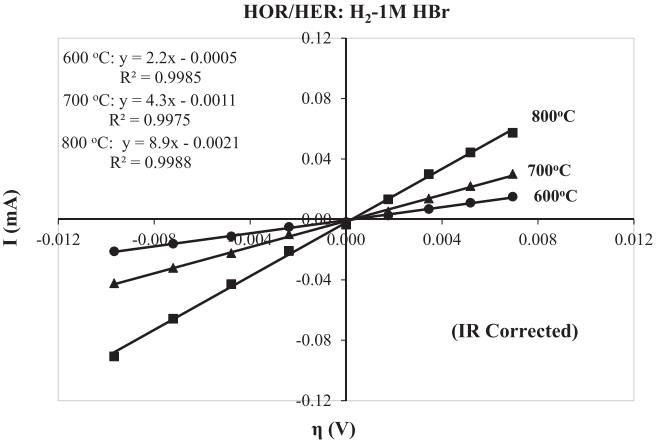

Figure 11. Linear plots of current density versus applied potentials of synthesized catalysts in H_2-saturated 1M HBr solution.

Table III. HER/HOR exchange current density of the catalysts in 1M H_2SO_4 and 1M HBr.

Catalyst	i_o in H_2SO_4 (mA/cm^2)	i_o* in H_2SO_4 (mA/ mg-Rh)	i_o in HBr (mA/cm^2)	i_o* in HBr (mA/ mg-Rh)
Precursor	-	-	-	-
600°C	0.89 ± 0.01	23.38 ± 0.48	0.81 ± 0.01	21.27 ± 0.48
700°C	0.92 ± 0.02	53.41 ± 1.16	0.81 ± 0.02	47.02 ± 1.17
800°C	1.04 ± 0.02	193.77 ± 3.71	0.92 ± 0.03	171.41 ± 5.59

Conclusions

We have successfully synthesized an active Rh_xS_y catalyst on carbon support with particle sizes between 3 and 12 nm. Thermal reduction of the inactive Rh_2S_3 phase created active phases of Rh_3S_4, $Rh_{17}S_{15}$ and Rh. Among the catalysts prepared, the catalyst synthesized at 800°C exhibited the highest ECSA as it contained the highest fraction of the active phases as confirmed by XRD and XPS analyses. The ECSA of these rhodium sulfide catalysts was found to decrease as the upper potential scan limit was extended beyond 0.65 V. This phenomenon might be attributed to the formation of rhodium hydrous oxide species which could not be reduced during the cathodic scan. The HOR/HER activity of the catalysts in H_2SO_4 and HBr solution were quantified as the exchange current density (i_0) per active area. The specific exchange current densities (i_0) in 1M H_2SO_4 (0.89 to 1.04 mA/cm^2) of Rh_xS_y/C catalysts are found to be comparable with Pt catalyst (1.0 to 1.2 mA / cm^2). The HER/HOR exchange current density in 1M HBr solution for the catalysts synthesized in the study are 0.81 ± 0.01 mA/cm^2, 0.81 ± 0.02 mA/cm^2, and 0.92 ± 0.03 mA/cm^2 for 600°C, 700°C and 800°C catalysts, respectively. The HER/HOR exchange current density of these catalysts may be lower in HBr than H_2SO_4 due to the adsorption of Br^- on the active surface. The highest mass specific activity i_o* was obtained with the catalyst synthesized at 800°C, due to the high active phase composition.

Acknowledgments

The work presented herein was funded in part by the Advanced Research Projects Agency-Energy (ARPA-E), U.S. Department of Energy, under Award Number DE-AR0000262. Authors are grateful to TVN Systems for its support of this work through a subcontract from TVN System.

References

1. C. G. Morales-Guio, S. D. Tilley, H. Vrubel, M. Gratzel, and X. Hu, *Nature Communications*, **5**, 3059 (2014).
2. T. Nguyen and R. Savinell, *Electrochemical Society Interface*, **19**(3), 54 (2010).
3. V. Yarlagadda and T. V. Nguyen, *J. Electrochem. Soc.*, **160**(6), F535 (2013).
4. J. Masud, M. T. Alam, Z. Awaludin, M. S. El-Deab, T. Okajima, and T. Ohsaka, *J. Power Sources*, **220**, 399 (2012).
5. Haley Kreutzer, Venkata Yarlagadda, and Trung Van Nguyen, *J. Electrochem. Soc.*, **159**(7), F331 (2012).
6. Trung Van Nguyen, Haley Kreutzer, Venkata Yarlagadda, Eric McFarland, and Nirala Singh, *ECS Transactions*, **53** (7), 75 (2013).
7. Kyu Taek Cho, Michael C. Tucker, Markus Ding, Paul Ridgway, Vincent S. Battaglia, Venkat Srinivasan, and Adam Z. Weber, *ChemPlusChem*, **79**, 1 (2014).
8. J. Lee, A. Ishihara, F. Dumeignil, K. Miyazaki, Y. Oomori, E. W. Qian, and T. Kabe, *J. Mol. Catal. A: Chemical*, **209**, 155 (2004).
9. J. R. Hayes, R. H. Bowker, A. F. Gaudette, M. C. Smith, C. E. Moak, C. Y. Nam, T. K. Pratum, and M. E. Bussell, *J. Catal.*, **276**, 249 (2010).
10. B. Rufus, V. Ramakrishnan, B. Viswanathan, and J. C. Kuriacose, *Langmuir*, **6**, 565 (1990).
11. R. W. Reeve, P. A. Christensen, A. J. Dickinson, A. Hamnett, and K. Scott, *Electrochim. Acta*, **45**, 4237 (2000).

12. D. Cao, A. Wieckowski, J. Inukai, and N. Alonso-Vante, *J. Electrochem. Soc.*, **153**, A869 (2006).
13. F. Gullá, L. Gancs, R. J. Allen, and S. Mukerjee, *Appl. Catal. A:General*, **326**, 227 (2007).
14. J. M. Ziegelbauer, A. F. Gullá, C. O'Laoire, C. Urgeghe, R. J. Allen, and S. Mukerjee, *Electrochim. Acta*, **52**, 6282 (2007).
15. J. M. Ziegelbauer, V. S. Murthi, C. O'Laoire, A. F. Gullá, and S. Mukerjee, *Electrochim. Acta*, **53**, 5587 (2008).
16. J. M. Ziegelbauer, D. Gatewood, A. F. Gullá, M. J. F. Guinel, F. Ernst, D. E. Ramaker, and S. Mukerjee, *J. Phys. Chem. C*, **113**, 6955 (2009).
17. C. Jin, W. Xia, T. C. Nagaiah, J. Guo, X. Chen, N. Li, M. Bron, W. Schuhmann, and M. Muhler, *J. Mater. Chem.*, **20**, 736 (2010).
18. C. Jin, T. C. Nagaiah, W. Xia, M. Bron, W. Schuhmann, and M. Muhler, *ChemSusChem*, **4**, 927 (2011).
19. Nirala Singh, John Hiller, Horia Metiu, and Eric McFarland, *Electrochimica Acta*, **145**, 224 (2014).
20. J. Masud, J. Walter, T. V. Nguyen, G. Lin, N. Singh, E. McFarland, H. Metiu, M. Ikenberry, K. Hohn, C. J. Pan, and B. J. Hwang, *ECS Trans*., **58** (37), 37 (2014).
21. R. J Allen and A. F Gulla, *U. S. Pat. 6,967,185 B2*, 22 Nov, 2005.
22. K. Lee, L. Zhang, and J. Zhang, *J. Power Sources*, **170**, 291 (2007).
23. B. Li, D. C. Higgins, D. Yang, H. Lv, Z. Yu, and J. Ma, *Int. J. Hydrogen Energy*, **38**, 5813 (2013).
24. W. Zhang, K. Yanagisawa, S. Kamiya, and T. Shou, *Crystal Growth & Design*, **9**(8), 3765 (2009).
25. N. R. B. M. Elezovic Babic, V. R. Radmilovic, and N. V. Krstajic, *J. Electrochem. Soc.*, **160** (10) F1151 (2013).
26. T. I. T. Okpalugo, P. Papakonstantinou, H. Murphy, J. McLaughlin, and N. M. D. Brown, *Carbon*, **43**, 153 (2005).
27. C. Jin, W. Xia, T. C. Nagaiah, J. Guo, X. Chen, N. Li, M. Bron, W. Schuhmann, and M. Muhler, *J. Mater. Chem.*, **20**, 736 (2010).
28. K. Matsumoto, T. Matsumoto, M. Kawano, H. Ohnuki, Y. Shichi, T. Nishide, and T. Sato, *J. Am. Chem. Soc.*, **118**, 3597 (1996).
29. D. Grumelli, C. Vercat, G. Benitez, M. E. Vela, and R. C. Salvarezza, *J. Phys. Chem. C*, **111**, 7179 (2007).
30. Y. Li, N. Li, K. Yanagisawa, X. Ding, X. Li, Y. Wei, and X. Yan, *J. Chem. Eng.*, **228**, 45 (2013).
31. J. M. Ziegelbauer, D. Gatewood, A. F. Gullá, D. E. Ramaker, and S. Mukerjee, *Electrochem and Solid-State Letters*, **9**(9), A430 (2006).
32. M. Goor-Dar, N. Travitsky, and E. Peled, *J. Power Sources*, **197**, 111 (2012).